Research Article | **Open Access**

Soft Science

Pan *et al*. *Soft Sci*. **2026**, *6*, 56 **DOI:**10.20517/ss.2026.23

Dual-frequency metastructured-hydrogel film for high-contrast ultrasound imaging

Zhangqi Pan[1,#], Bo Gao[1,#], Yuli Li[1], Ye Tian[1], Jianfeng Zang[1,2,*], Hanchuan Tang[1,*]

Keywords:
Acoustic metamaterial, ultrasound imaging, contrast, hydrogel, dual-frequency

Citation: Pan, Z.; Gao, B.; Li, Y.; Tian, Y.; Zang, J.; Tang, H. Dual-frequency metastructured-hydrogel film for high-contrast ultrasound imaging. *Soft Sci.* **2026**, *6*, 56. https://dx.doi.org/10.20517/ss.2026.23

Received: 30 Jan 2026
First Decision: 22 Apr 2026
Revised: 21 May 2026
Accepted: 22 May 2026
Published: 2 Jul 2026

Academic Editors:
Yu Song, Xinge Yu
Copy Editor:
Xing-Yue Zhang
Production Editor:
Xing-Yue Zhang

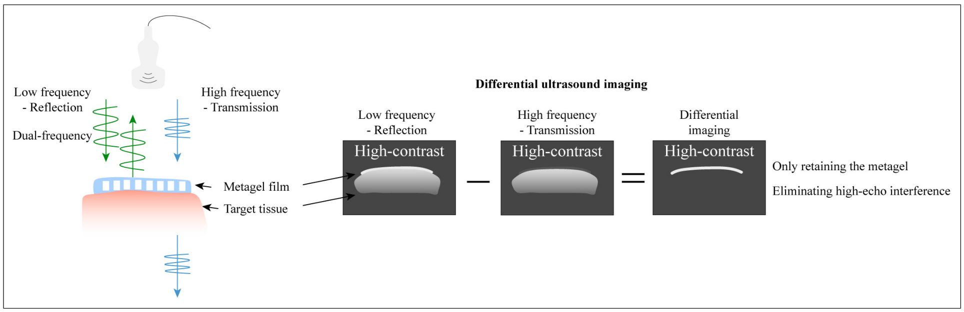

Abstract

Contrast agents enhance the resolution and clarity of ultrasound imaging, thereby improving the accuracy of diagnosis and treatment. However, the imaging performance of existing contrast agents is limited by the non-specificity of B-mode ultrasound imaging, particularly when high-echo tissue interference is present. Here, we propose a metastructured hydrogel (metagel) film with a steep reflectance transition at a specific frequency, enabling differential imaging between the higher and lower frequencies to suppress background interference. The ultrasonic reflection field is investigated for parameter optimization. The metagel film exhibits shape-retaining properties, demonstrating approximately 4 times reflectivity contrast within a 40% strain range. Through a customized dual-frequency excitation mode combined with ultrasonic spectrum analysis, we propose a dual-frequency differential imaging workflow. Compared with the reflection amplitude of zinc metal, our method achieves a signal-to-noise ratio exceeding 50 dB and a 4 times signal enhancement. Combined with an adhesive hydrogel patch, we demonstrate the conformal and imaging enhancement capabilities of the metagel film on complex surfaces, providing an effective tool for interference-free ultrasound imaging.

---

[1]School of Integrated Circuits and Wuhan National Laboratory for Optoelectronics, Huazhong University of Science and Technology, Wuhan 430074, Hubei, China.
[2]The State Key Laboratory of Intelligent Manufacturing Equipment and Technology, Huazhong University of Science and Technology, Wuhan 430074, Hubei, China.
[#]Authors contributed equally.

[*]**Correspondence to:** Prof. Jianfeng Zang, Prof. Hanchuan Tang, School of Integrated Circuits and Wuhan National Laboratory for Optoelectronics, Huazhong University of Science and Technology, Wuhan 430074, Hubei, China. E-mail: jfzang@hust.edu.cn; hctang1@hust.edu.cn

INTRODUCTION

Visualizing the location, morphology, and function of specific organs and tissues within the body is crucial for disease monitoring, management, and treatment[1]. Currently, multiple mature imaging modalities are applied, including fluorescence imaging, ultrasound imaging, magnetic resonance imaging (MRI), computed tomography (CT), and positron emission tomography (PET)[2]. To overcome the physical limitations of existing imaging technologies, contrast agents have been developed to enhance signal contrast and imaging resolution. They have found extensive application in cross-scale target imaging, encompassing blood vessels, body cavities, and other structures[3].

Among various imaging technologies, ultrasound imaging is the most widely used due to its radiation-free nature, high penetration depth, cost-effectiveness, and ease of operation[4-6]. However, its resolution, particularly in deep tissues, is relatively low on the order of millimeters[7]. Furthermore, traditional B-mode ultrasound imaging encodes spatial information through the amplitude of reflected ultrasound waves, relying on grayscale information to identify imaging targets. Due to this inherent non-specificity, any high-echo tissue within the body can generate signal interference that obscures the imaging target. Consequently, the success of ultrasound-based diagnosis and treatment often heavily depend on the physician's experience[8].

To enhance ultrasound imaging, oral or injectable microbubble contrast agents are commonly used. These agents amplify the amplitude of ultrasound echo signals by strongly reflecting acoustic waves through gas bubbles[9-11]. However, when circulating in the bloodstream, such contrast agents may pose risks or exhibit physiological toxicity[9-10]. Furthermore, they also lack ultrasound specificity and do not fundamentally eliminate image artifacts caused by high-echo tissues[11].

Acoustic metamaterials are a class of materials that flexibly manipulate acoustic waves through structural design, exhibiting novel acoustic properties[12-14]. They are utilized in subwavelength imaging[15-17], acoustic holography[18-20], and acoustic absorption[21-23]. By embedding submillimeter air cavity scatterers within hydrogel materials, an acoustic metastructured hydrogel (metagel) can be constructed, achieving applications in ultrasonic impedance tuning[24-28]. Here, we developed an acoustic metagel film exhibiting a step-like acoustic spectral characteristic. Compared to non-specific imaging targets, it demonstrates a significant contrast in reflectivity across relatively high and low acoustic frequency bands. Utilizing a dual-frequency ultrasound probe, differential imaging in the frequency domain eliminates interference from high-echo tissues, enabling high-contrast ultrasound imaging. To optimize design parameters, we performed computational modeling of the ultrasonic reflection acoustic field. The metagel film maintains performance under deformation, achieving approximately 4 times reflectivity contrast enhancement across a 40% strain range. By designing dual-frequency excitation modes and integrating ultrasonic spectral analysis, we investigated reflectivity differences between the metagel film and zinc tablet during dual-frequency imaging, achieving a signal-to-noise ratio exceeding 50 dB and a 4 times amplification of the reflected ultrasonic signal amplitude. Furthermore, using adhesive hydrogel patches, we demonstrated the metagel film's conformal attachment and imaging enhancement capabilities on complex curved surfaces, thereby providing an effective tool for interference-free ultrasound imaging.

EXPERIMENTAL

Simulation

Finite-element analysis was conducted to simulate acoustic fields around the metagel in COMSOL Multiphysics 6.0. Free-triangular-mesh elements were used with a maximum size of 0.02 mm ($< \lambda/10$ for 6 MHz ultrasonic waves). Hydrogels were modeled using hyperelasticity for the simulation of ultrasonic wave propagation. The bulk modulus was calculated at 2.21 GPa (equivalent to water at 25 °C), and the density was calculated at 1 g/cm^3.

Metagel fabrication

First, a mold containing periodic column structures was designed using SolidWorks software (Dassault Systèmes, USA). Subsequently, a template was fabricated via photopolymerization 3D printing (NanoArch S140, BMF Precision Material Technology, Inc., China). Poly(vinyl alcohol) (PVA) (124) particles were stirred at 90 °C for 1 h and dissolved in deionized water. After standing for 24 h, the PVA hydrogel precursor solution was obtained and carefully poured into the mold. After three cycles of freeze-thawing at -20 °C for 23 h and 25 °C for 1 h, an open-pored hydrogel structure was obtained. A thin film of the hydrogel precursor (approximately 0.1 mm thick) was spin-coated. The resulting open-pored hydrogel structure was placed on top of this precursor film. Following two additional freeze-thaw cycles and removal of excess structure, the metagel sample was obtained.

Double-sided adhesive hydrogel fabrication

Add 3% (w/w) AAc-NHS ester, 30% (w/w) acrylic acid, 0.1% (w/w) N, N’-methylenebisacrylamide, 0.2% (w/w) photoinitiator Lap, and 4% (w/w) VBTMA to deionized water until completely dissolved. Pour the precursor solution into a PTFE mold (0.5 mm depth) and cover with a piece of quartz glass. Cure for 30 min in a UV chamber (365 nm). Then dry for 15 min in a circulating air oven at 60 °C to prepare the bioadhesive hydrogel.

Mechanical tests

To measure Young’s modulus, dog-bone-shaped specimens were prepared with initial dimensions of 5 mm width, 0.8 mm thickness, and a gauge length of 10 mm. Testing was conducted on a tensile testing machine (RGM-6005, REGER) equipped with a 20 N load cell at a strain rate of 0.01 s^{-1}. Stress-strain curves were plotted for each specimen, and Young’s modulus was determined from the initial slope. To measure adhesion energy, the bioadhesive hydrogel was bonded to porcine intestine and subjected to a 180-degree peel test using the tensile testing machine (RGM-6005, REGER). All data were averaged and expressed as mean ± SD based on three independent measurements ($n = 3$). Porcine tissues were purchased from a local slaughterhouse (COFCO Joycome Foods Limited, Wuhan, China).

Dual-frequency ultrasonic probe

A dual-frequency ultrasonic probe was customized and purchased from Suzhou Norayso Technology Co., Ltd. Its schematic diagram is shown in Supplementary Figure 1, featuring two sets of piezoelectric elements with different resonant frequencies for emitting ultrasonic waves at 2 and 6 MHz, respectively. The intrinsic spectrum of this probe is depicted in Supplementary Figure 2 and parameters of the equipment used in this work are listed in Supplementary Table 1.

Differential imaging

Ultrasonic waves at 2 and 6 MHz are transmitted and received sequentially. For example, when the the pulse repetition frequency (PRF) is 4,000, 4,000 echoes are transmitted per second, or one echo every 0.25 ms. Thus, the 2 and 6 MHz ultrasonic waves switch at this frequency. The differential ultrasound imaging mode directly processes RF data, converting the amplitude of the line scan into ultrasound pixels in the vertical direction, while the scan lines are distributed horizontally to form a two-dimensional image. The raw data are normalized, and differential ultrasound imaging is obtained by subtracting the 2 MHz ultrasound data matrix from the 6 MHz ultrasound data matrix.

RESULTS AND DISCUSSION

The schematic structure of the metagel film is shown in Figure 1A, where a periodically arranged air-cell array is embedded within the hydrogel. At a specific frequency (termed the “cutoff frequency”), the reflectivity decreases sharply. Consequently, when ultrasound waves are incident on the metagel,

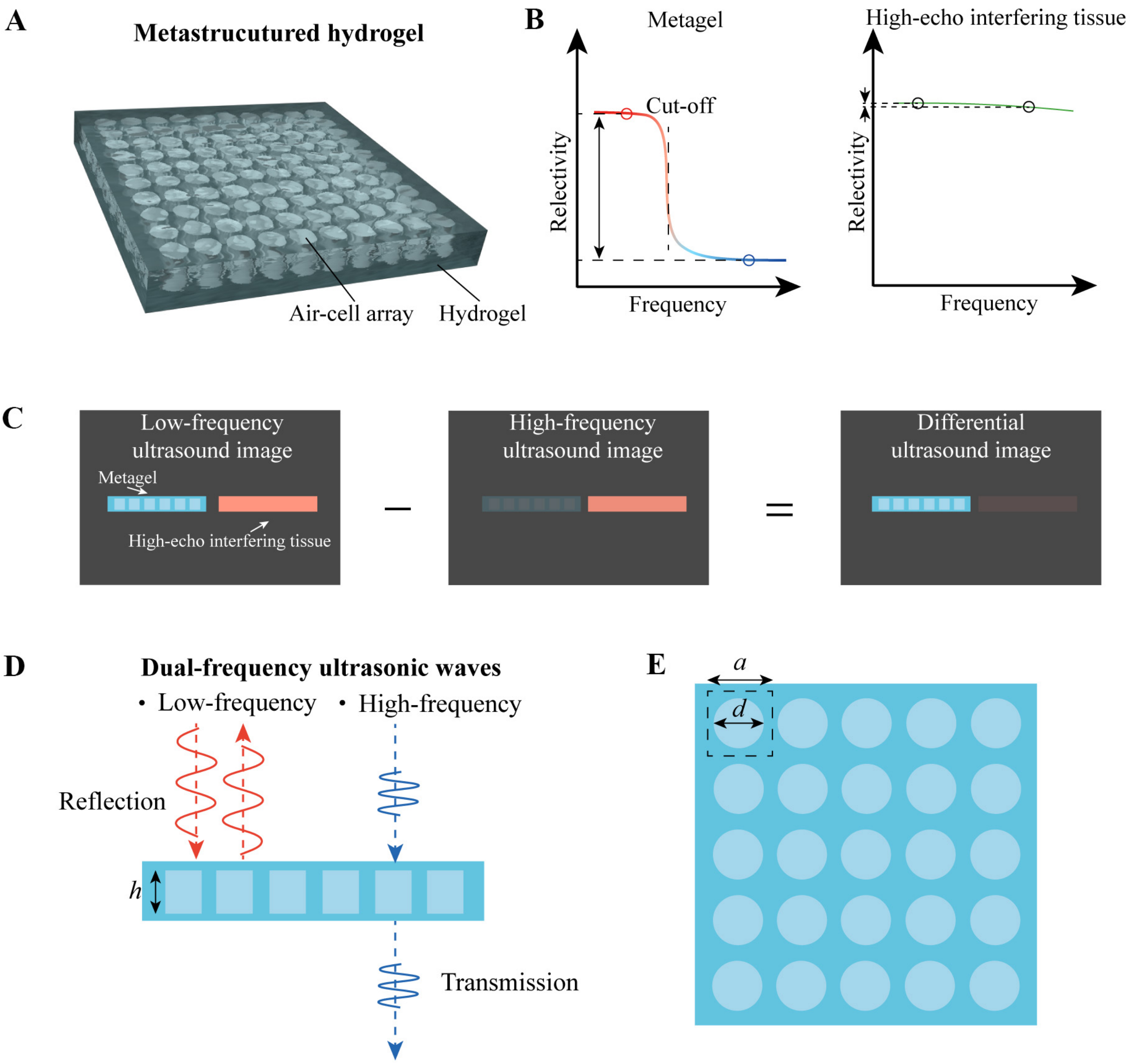

Figure 1. Schematic of the metagel film. (A) Schematic of the metagel film with periodically arranged air-cells within the hydrogel; (B) Schematic of the metagel reflection spectrum, showing a steep decrease in reflectivity at the cutoff frequency and a significant contrast across high and low frequency ranges; (C) Schematic of differential imaging, which achieves high contrast to eliminate interference from high-echo tissues; (D) Schematic of dual-frequency ultrasound excitation mode, in which low-frequency ultrasound is reflected while high-frequency ultrasound is transmitted. The height of the air-cell scatterer is denoted as *h*; (E) Geometric parameters influencing metagel performance, including the diameter *d* of the air-cell scatterer and the lattice constant *a*.

lower-frequency acoustic waves are reflected while higher frequencies are transmitted [Figure 1B], which is a unique characteristic not found in human tissue or other conventional imaging targets. Therefore, by performing a differential operation between the relatively low-frequency image and the relatively high-frequency image, interference from any other tissue can be eliminated, thereby clearly preserving the metagel film itself [Figure 1C].

This unique property is attributable to the arrangement of the air cells. Each air cell is cylindrical with a uniform diameter d, occupies individual lattice sites with a lattice constant denoted as a and with a height denoted as h [Figure 1D and E]. According to the acoustic wave propagation equation:

$$\nabla^2 P - \frac{\rho}{B}\frac{\partial^2 P}{\partial t^2} = 0 \tag{1}$$

The velocity of sound in different media is determined by the medium's properties: $v = \sqrt{\frac{B}{\rho}}$. In the Equation (1), P represents the acoustic pressure field, ρ and B denote the density and bulk modulus of the medium, respectively. Therefore, the primary parameters affecting the refractive index of acoustic waves between different materials are bulk modulus and density. Owing to the high water content (> 90%) of hydrogels, their bulk modulus and density are similar to those of water. In contrast, the bulk modulus of air cells is significantly lower than that of water, leading to strong scattering at the air-hydrogel interface. Moreover, the periodic arrangement of air cells forms a lattice structure, which induces Bragg scattering. This creates an acoustic bandgap analogous to that in crystalline structures, resulting in novel frequency-domain characteristics.

We conducted simulations to validate this principle (see Supplementary Figure 3 in Supplementary Materials for the simulation physics field settings). For a metagel with lattice constant $a = 0.55$, diameter d/a (denoted as filling ratio q) = 0.55, and h = 1 mm, the ultrasonic wave at 2 MHz undergoes focused reflection [Figure 2A], while the ultrasonic wave at 6 MHz is largely transmitted. The non-transmitted ultrasonic wave also scatters in surrounding directions [Figure 2B]. Its specific spectrum is shown in Figure 2C, with a cutoff frequency occurring at approximately 4.5 MHz. We also compared the reflected ultrasound spectra of other materials, including high-scattering bone and low-scattering soft tissue. Their reflection amplitude decreases slightly with increasing ultrasound frequency, which is attributed to the inherent attenuation of high-frequency ultrasound, resulting in a smooth reflection spectrum without a distinct step-like drop. Therefore, when high- and low- ultrasonic waves are simultaneously incident upon the metagel films and human organs, the metagel exhibits a distinct difference in reflection intensity, whereas human organs do not. Ultimately, by processing the amplitude of acoustic waves at different frequencies, the interfering acoustic field from high-echo tissues can be eliminated.

This peculiar mechanism can be explained by multiple scattering[24]. When acoustic waves pass through a periodically arranged scattering structure (such as the air cells in a metagel), each scatterer causes scattering of the incident wave. These scattered waves then interact with each other again, creating a multiple scattering effect, which can be explained as follows:

The incident plane wave is expressed as:

$$P = e^{iky} \tag{2}$$

where k denotes the wave vector, and y represents the direction of ultrasonic incidence (simplified as normal incidence). Expressing Equation (2) as an expansion of a Hankel function of the first kind gives:

$$P_{j,l} = \sum_{n=-\infty}^{\infty} B_n^{(j,l)} H_n\left(kr_{j,l}\right) e^{in\theta_{j,l}} \tag{3}$$

The Equation (3) represents the scattered ultrasound from the l^th^ scatterer in the j^th^ incident cycle. $B_n^{(j,l)}$ is the scattering coefficient, H_n denotes the first-class Hankel function, $(r_{j,l}, \theta_{j,l})$ are the polar coordinates centered on this scatterer. Due to the periodicity of the metagel structure, scatterers at the same position are simplified to have the same scattering coefficient.

The total scattering field is expressed as:

$$P^{\text{total}} = \sum_{j=-\infty}^{\infty} \sum_{p=1}^{N} P_{j,l} \tag{4}$$

Further expand Equation (4) as a sum of plane waves of different diffraction orders:

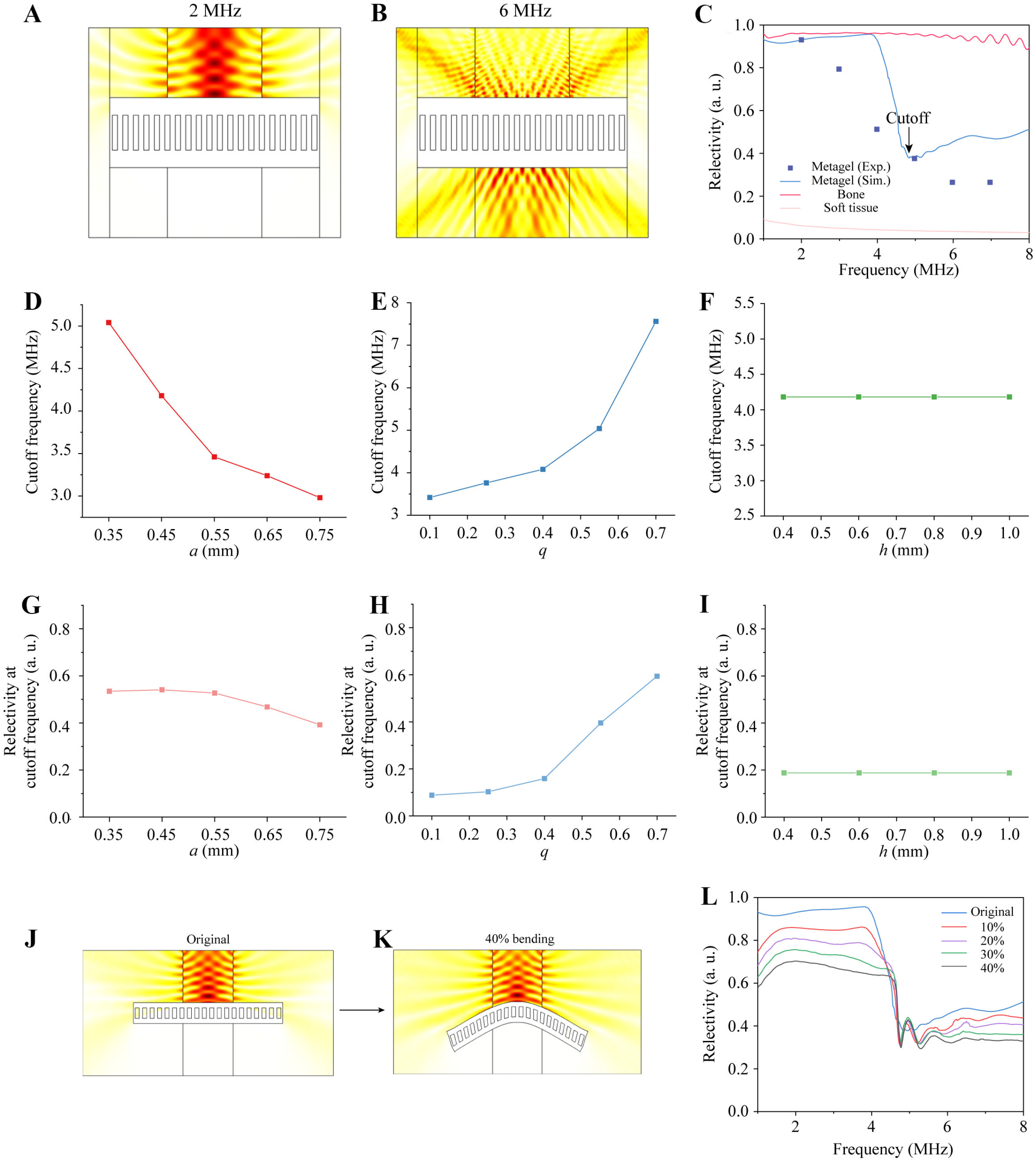

Figure 2. Ultrasonic reflection of the metagel film. Simulation results of acoustic field distribution (A) at 2 MHz and (B) at 6 MHz; (C) Ultrasonic reflection spectra of the metagel. Parameter effects on cutoff frequency of (D) lattice constant *a*, (E) filling ratio *q* and (F) air-cell height *h*. Parameter effects on reflectivity at cutoff frequency of (G) *a*, (H) *q* and (I) *h*; (J) Ultrasonic reflection without deformation and (K), with 40% bending deformation; (L) Ultrasonic reflection spectra with different degrees of deformation.

$$P^{\text{total}} = \sum_{n=-\infty}^{\infty} P_n e^{(ik\cos\theta_n x + ik\sin\theta_n |y|)} \tag{5}$$

where, $\cos\theta_n = n\frac{2\pi}{kNa}$, N denotes the total number of scatterers.

For the n$^{\text{th}}$-order scattered wave, the transmission coefficient T_n and reflectance coefficient R_n are given by[24]:

$$\begin{aligned} R_n &= \frac{2}{ka\sin\theta_n}\sum_{q=1}^{N} e^{\left(-i\frac{2n\pi}{Na}R_{0,q}\right)}\sum_{m=-\infty}^{\infty} B_m^q(-i)^m e^{im\theta_n} \\ T_n &= 1 - \frac{2}{ka\sin\theta_n}\sum_{q=1}^{N} e^{\left(-i\frac{2n\pi}{Na}R_{0,q}\right)}\sum_{m=-\infty}^{\infty} B_m^q(-i)^m e^{im\theta_n} \end{aligned} \tag{6}$$

For the principal reflection order, i.e., when $n = 0$[24]:

$$R_0 = \frac{2}{ka}\sum_{n=-\infty}^{\infty}(-1)^n B_n \tag{7}$$

Therefore, as seen from Equation (7), the reflectivity is inversely proportional to a. This is related to the bandgap properties of Bragg scattering-type acoustic metamaterials, where ultrasonic waves at the bandgap center frequency possess wavelengths similar to the lattice constant. That is to say, a larger lattice constant results in a lower characteristic reflection frequency (corresponding to the cutoff frequency for the metagel). The following relationship holds[29]:

$$f_{cutoff} \sim n\frac{v}{2a} \tag{8}$$

We investigated the influence of different design parameters on the reflective properties of the metagel. As shown in Figure 2D, a larger lattice constant leads to a lower cutoff frequency, consistent with the conclusion derived from Equation (7). Simultaneously, the cutoff frequency increases with increasing fill factor, as depicted in Figure 2E. The height of the air cells within the metagel has a negligible impact on the cutoff frequency [Figure 2F].

Furthermore, we investigated the ultrasonic reflectivity at the cutoff frequency, which reflects the ratio of high-frequency (above cutoff frequency) to low-frequency (below cutoff frequency) ultrasonic reflectivity. As shown in Figure 2G-I, to ensure contrast between high- and low-frequency ultrasonic waves, a relatively high air-cell filling ratio and a small lattice constant are typically required. However, smaller dimensions pose manufacturing challenges and necessitate careful consideration in practical applications. The reflection spectra for each parameter are presented in Supplementary Figure 4. Therefore, the design of the metagel film can be scaled to accommodate ultrasonic transducers with different center frequencies [Supplementary Figure 5].

Due to the typically convoluted and non-planar nature of internal organs, conformal issues must be considered when using metagels as solid imaging films. Therefore, we investigated the ultrasonic reflection spectra under different strains, as shown in Figure 2J and K. Even at 40% bending strain, the metagel maintains strong reflection at low frequencies. The reflection spectra under various bending strains are depicted in Figure 2L. The cutoff frequency and reflectivity at this frequency remain nearly constant, while both high- and low-frequency reflectivities decrease. This reduction stems from deformation-induced performance loss but does not affect the contrast ratio, which remains high at approximately 4 times.

To further validate the imaging performance of the metagel film, we prepared metagel samples for testing. Using a single probe [Supplementary Figures 1 and 2] to simultaneously emit ultrasonic waves at two frequencies - 2 and 6 MHz - a technique termed dual-frequency scanning, we compared the reflection spectra of the metagel, pure hydrogel (without an air-cell structure, same thickness as the metagel), and zinc metal. As a high-echo material, zinc can be used in ultrasound imaging. Therefore, we selected zinc as an extremely high-echo interference source. As shown in Figure 3A and B, the metagel exhibits significant difference in peak reflection amplitude between 6 and 2 MHz frequencies, whereas the highly reflective zinc and the low-reflective pure gel remain nearly unchanged. Therefore, when subtracting the 6 MHz ultrasonic signal from the 2 MHz signal, the difference signals for zinc and pure gel approach zero, whereas the metagel

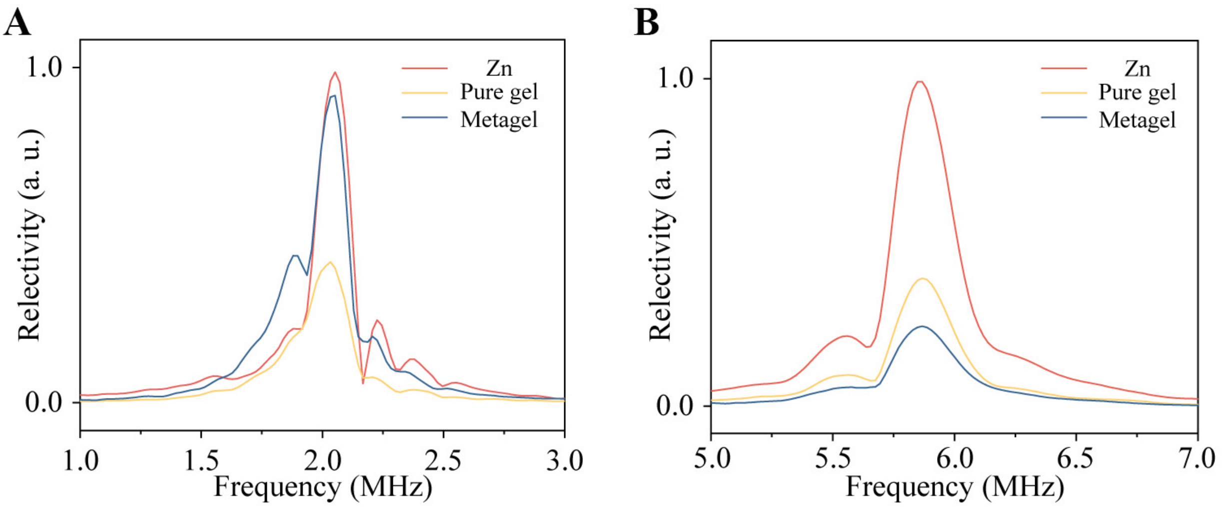

Figure 3. Spectra of the metagel, pure gel and zinc metal by dual-frequency ultrasound scanning at (A) 2 MHz and (B) 6 MHz. Compared to zinc metal and pure gel, the metagel exhibits a greater difference in reflectivity under excitation at 6 and 2 MHz.

signal is only partially subtracted, with most components retained. This principle forms the basis for eliminating high-echo interference through dual-frequency scanning. In addition, the metagel maintains stable reflective performance at various depths, up to 10 cm [Supplementary Figure 6]. During a 7-day continuous stability test, the metagel also maintained good performance [Supplementary Figure 7].

For the dualfrequency differential imaging proposed in this work, the identification of the metagel film relies primarily on frequency specificity. Therefore, in the axial direction, data containing the echo information of the entire object must be acquired to process a complete frequency spectrum, meaning that the axial resolution is comparable to the size of the device itself, approximately 1 mm. The lateral resolution is equal to the interval between line-scan ultrasonic transducer elements (0.15 mm). In contrast, traditional microbubble ultrasound contrast agents have a lateral resolution of approximately 2 mm and an axial resolution of 1 mm[3].

Based on the above mechanism, we established a differential ultrasound imaging mode, as shown in Figure 4. A single ultrasound radiofrequency (RF) echo signal is converted into a digital signal, with the number of sampling points denoted as n. By performing spatial line scanning, m lines of RF data are acquired, yielding a 2D raw image matrix. The matrix element $a_{i,j}$ is normalized and converted to grayscale intensity $b_{i,j}$. By subtracting the two sets of grayscale images $b_{i,j}$ and $c_{i,j}$ obtained from dual-frequency scanning (high and low frequencies, respectively), the image of the metagel film itself is preserved while images of other tissues are eliminated, thereby achieving high-contrast ultrasound imaging.

We demonstrate the practical application of this imaging modality. As shown in Figure 5A, a dual-frequency ultrasound probe simultaneously emits 2 and 6 MHz ultrasound waves to acquire echoes from a zinc tablet, pure gel, and metagel. These echoes are uniformly processed into ultrasound grayscale images, as depicted in Figure 5B-D. In the 2 MHz center-frequency ultrasound image, both the highly reflective zinc and metagel are visible. However, in the 6 MHz image, the metagel film exhibits low reflectivity due to its inherent spectral characteristics, resulting in an image that only reveals the zinc. Given inherent resolution differences in both 2 and 6 MHz ultrasound imaging, regions of interest (ROIs) were selected in the higher-resolution 6 MHz ultrasound images and delineated in the corresponding 2 MHz images, while the remaining areas are still processed according to the original 6 MHz image. In practice, this approach allows both accurate localization of the implant and preservation of the higher-resolution 6 MHz ultrasound images of the

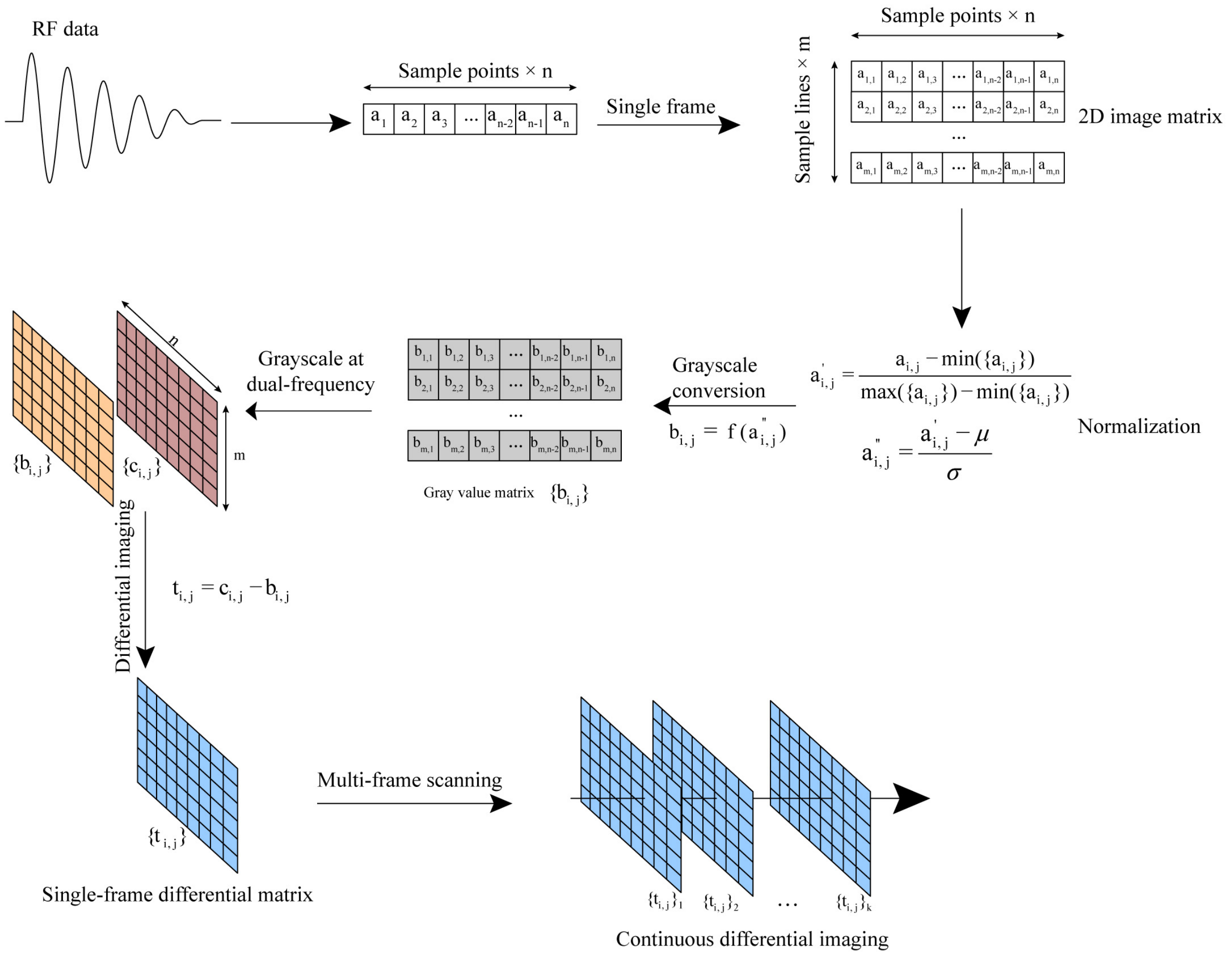

Figure 4. Differential ultrasound imaging algorithm based on dual-frequency scanning.

internal body structures. Differential imaging processing applied to these overlapping regions yielded the differential image shown in Figure 5D. The high-echo interference from the zinc tablet is nearly eliminated, leaving only the high-gray-value image of the metagel film, thereby achieving the objective of high-contrast ultrasound imaging. Specifically, the 2 MHz ultrasound imaging shown in Figure 5B corresponds to the previously reported metagel imaging method, i.e., using a metagel with a single-layer periodic air-column structure and directly performing ultrasound imaging at a center frequency of 2 MHz[26].

We performed quantitative analysis of this imaging modality. Figure 5E demonstrates that the metagel film achieves a signal-to-noise ratio (i.e., the dB value above the noise signal) as high as 50 dB in dual-frequency differential imaging. Statistical analysis was conducted using Student's t-test. For the metagel film, a significant difference was observed between the 2M and differential images ($P = 0.0003$). For zinc tablet, no significance (NS) was observed between the 2M and differential images ($P = 0.3882$). The signal-to-noise ratio further improves with repeated cyclic excitation of the dual-frequency probe [Figure 5F]. Compared to the grayscale image of the high-intensity reflector zinc, the metagel film exhibits 4 times increase in signal amplitude contrast [Figure 5G, Supplementary Table 2].

Given that hydrogels are inherently polymeric materials capable of flexible modification, they can be endowed with additional functionalities to serve diverse application scenarios. Here, we leverage the adhesive properties of hydrogels to achieve conformal attachment of metagels, further meeting the requirements for *in vivo* ultrasound imaging applications [Figure 6A]. We incorporated -NHS esters into the hydrogel to create a

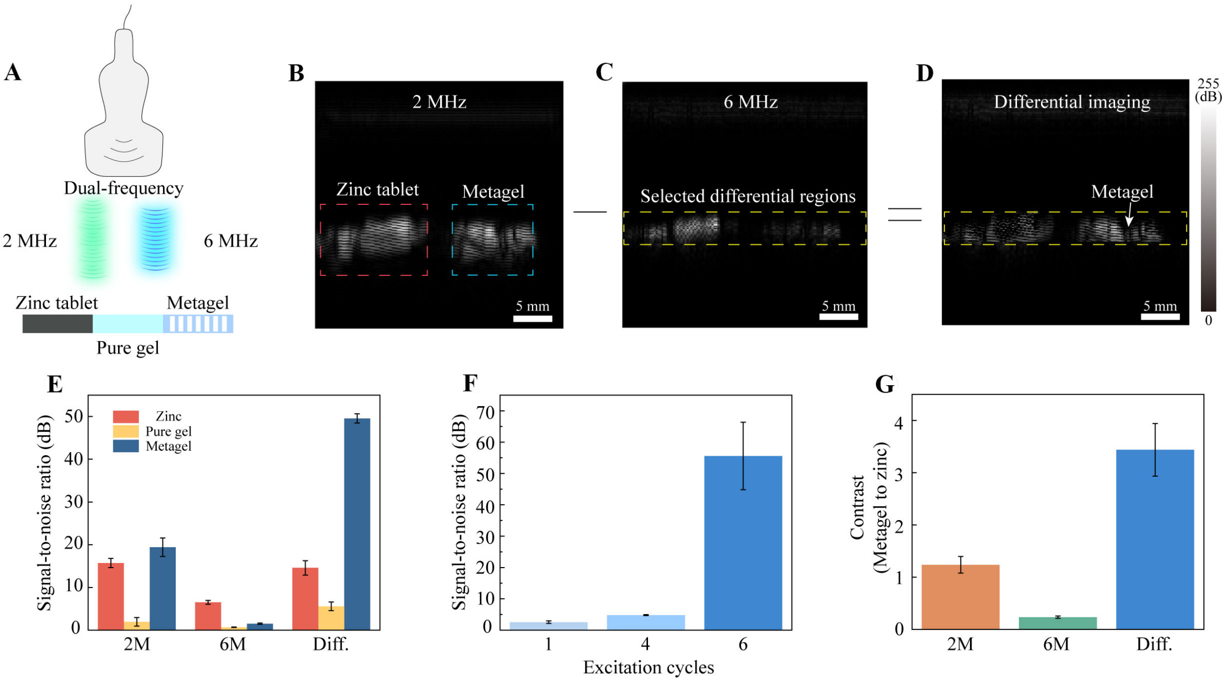

Figure 5. Demonstration of the differential ultrasound imaging of the metagel film. (A) Simultaneous dual-frequency excitation of the zinc tablet, pure gel, and metagel. Ultrasound images are shown in (B) at 2 MHz, (C) at 6 MHz and (D) after differential processing. In the differential image, most of the interfering echoes other than those from the metagel film have been suppressed; (E-G) Statistical analysis of the differential imaging ($n = 3$); (E) Signal-to-noise ratio for 2 MHz B-mode/6 MHz B-mode/differential ultrasound imaging of zinc/pure gel/metagel; (F)Signal-to-noise ratio differential ultrasound imaging of the metagel film; (G) Contrast for 2 MHz B-mode/6 MHz B-mode/differential ultrasound imaging. Data are represented as mean value ± SD (standard deviation). Three independent tests were conducted ($n = 3$).

double-sided adhesive hydrogel patch[30]. Amines introduced into the metagel film bonded to the adhesive layer. Similarly, proteins in the human body, rich in amino groups, also bonded effectively to the adhesive layer, as shown in Figure 6B. The adhesion performance of the adhesive layer at both interfaces is illustrated in Figure 6C. We adhered the metagel film to surfaces of three distinct shapes - C-, S-, and M-shaped [Figure 6D] - and imaged these objects, demonstrating the metagel film's excellent conformal and high-contrast imaging capabilities. Considering the material's ability to maintain its properties under deformation [Figure 2J-L], its flexible nature, and its adhesive properties, the conformal imaging performance of the metagel film is expected to be excellent. Using the following parameters: PRF = 4,000, scan line = 128, and pulse cycle = 6, the temporal resolution of differential imaging is calculated to be 37 frame per second (FPS), which is expected to effectively resist motion artifacts. Owing to the material's ability to maintain its properties under deformation, the change in performance caused by the pressure dissipated from the external probe to the interior is negligible.

Due to the complexity of the internal environment, various tissues including fibrous tissue, connective tissue, and cartilage appear as high-echo structures in ultrasound images, thereby interfering with the physician's assessment of the imaged area. Among these, bone exhibits strong acoustic reflection properties comparable to metal. Therefore, we further applied the metagel film to an *ex vivo* porcine rib tissue specimen, which simultaneously contains both high-echo (bone) and low-echo (fat and muscle, *etc*.) regions. Through dual-frequency differential imaging, we achieved high-contrast enhancement of the metagel film [Figure 6E]. This demonstrates that our metagel film not only conforms to complex human tissue geometries but also enables high-contrast imaging, effectively suppressing interference from strong echo signals - a unique capability unattainable with existing contrast agents. This fundamentally eliminates background interference

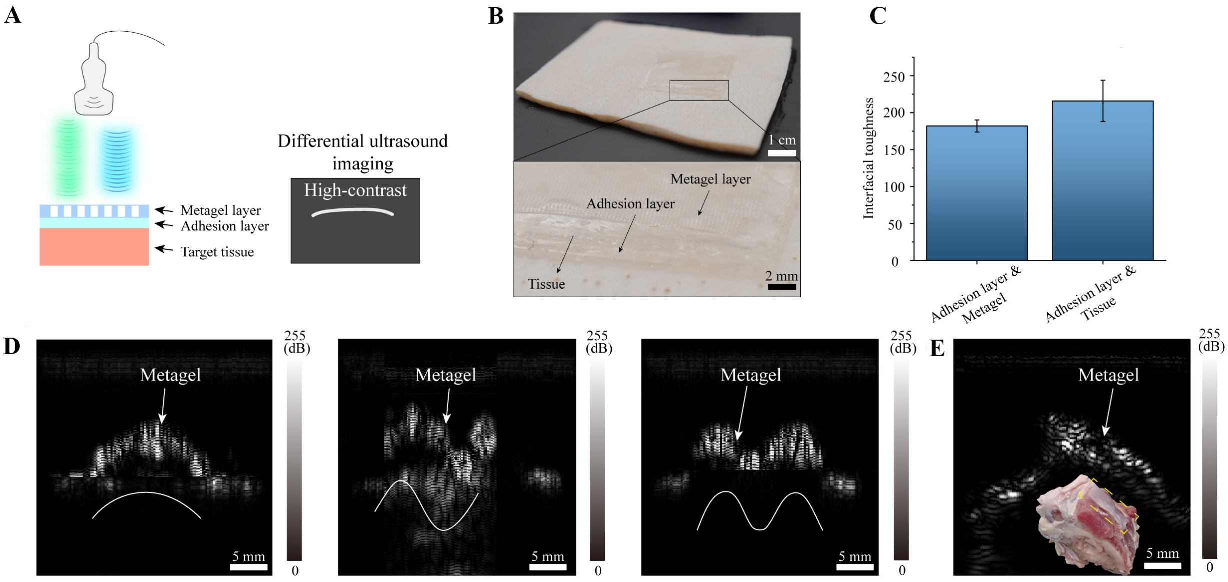

Figure 6. Ultrasound contrast application of the metagel film. (A) Schematic of a metagel conformally attached to soft tissue via an adhesion layer, enabling high-contrast imaging through dual-frequency excitation; (B) Photograph of the metagel film adhering to soft tissue; (C) Adhesion strength between the adhesion layer and the metagel film, and between the adhesion layer and tissue. Data are represented as mean value ± SD (standard deviation). Three independent tests were conducted (*n* = 3); (D) Dual-frequency differential imaging of the metagel film conformally adhered to various curved surfaces; (E) Dual-frequency differential imaging of the metagel film adhered to *ex vivo* tissue containing both soft and hard components.

through acoustic specificity. In addition, the swelling ratio of the metagel film is as low as 20%, which effectively minimizes performance degradation caused by swelling and deformation, and it can be stabilized by a 48-hour pre-swelling process [Supplementary Figure 8].

CONCLUSION

Our research proposes a high-contrast metagel film based on the acoustic modulation capabilities of flexible acoustic metamaterials. By leveraging the contrast between high- and low-frequency ultrasound echo signals, it eliminates echo interference from normal imaging targets, resulting in signal enhancement that surpasses that of metallic reflectors. The ultrasound imaging performance of the metagel film has been comprehensively validated through theoretical analysis, simulation calculations, and experimental testing. Composed entirely of hydrogel, the metagel film exhibits exceptional flexibility, biocompatibility, and complete biodegradability. Its integration with adhesive hydrogels further demonstrates the metagel film's targeted imaging capabilities for specific tissues. The proposed metagel film not only overcomes the short duration of action associated with traditional microbubble contrast agents but also enables specific localization by eliminating high-echo backgrounds [Supplementary Table 3]. Our approach not only serves imaging device development and clinical research but also opens new avenues in soft materials, metamaterials, and applied acoustics.

DECLARATIONS

Authors' contributions

Data curation, formal analysis, investigation, software, validation, visualization, writing - original draft: Pan, Z.
Data curation, formal analysis, investigation, fabrication: Gao, B.
Data curation, investigation: Li, Y.
Methodology, conceptualization: Tian, Y.
Resources, supervision, writing - review and editing: Zang, J.
Funding acquisition, resources, supervision, writing - review and editing: Tang, H.

Availability of data and materials

The data that support the findings of this study are available from the corresponding authors upon reasonable request.

AI and AI-assisted tools statement

During the preparation of this manuscript, the AI tool DeepSeek (version R1, released 2025-May) was used solely for language editing. The tool did not influence the study design, data collection, analysis, interpretation, or the scientific content of the work. All authors take full responsibility for the accuracy, integrity, and final content of the manuscript.

Financial support and sponsorship

This work is supported by the National Key Research and Development Program of China [No. 2024YFB4614400] (Zang, J., Tang, H.), the National Natural Science Foundation of China [No. T2350001] (Zang, J., Tang, H.), and [No. 82572372] (Tang, H.), Natural Science Foundation of Wuhan [No. 2025040601020218] (Tang, H.), the Young Elite Scientists Sponsorship Program by China Association of Science & Technology [No. 2024QNRC001] (Tang, H.), the HUST Interdisciplinary Research Project [No. 2023JCYJ044] (Tang, H.), and the Fundamental Research Funds for the Central Universities, HUST [No. 2025JYCXJJ037] (Pan, Z.).

Conflicts of interest

All authors declared that there are no conflicts of interest.

Ethical approval and consent to participate

Porcine tissues were purchased from a local slaughterhouse (COFCO Joycome Foods Limited, Wuhan, China). No animal tissues were specifically purchased or processed for research purposes. *Ex vivo* tissues were obtained through commercial channels. Therefore, ethical approval for animal experimentation is not required.

Consent for publication

Not applicable.

Copyright

Supplementary Materials

Supplementary Materials

REFERENCES

1. Wang, C.; Chen, X.; Wang, L.; et al. Bioadhesive ultrasound for long-term continuous imaging of diverse organs. *Science* **2022**, *377*, 517-23. DOI PubMed
2. Zhai, R.; Pan, Z.; Kou, Y.; et al. Multi-frequency dual-echo magnetic resonance imaging for real-time and artifact-free magnetic robot navigation. *Engineering* **2026**, *57*, 189-99. DOI
3. Dan, Q.; Jiang, X.; Wang, R.; Dai, Z.; Sun, D. Biogenic imaging contrast agents. *Adv. Sci.* **2023**, *10*, 2207090. DOI PubMed PMC
4. Lin, M.; Zhang, Z.; Gao, X.; et al. A fully integrated wearable ultrasound system to monitor deep tissues in moving subjects. *Nat. Biotechnol.* **2023**, *42*, 448-57. DOI PubMed
5. Hu, H.; Ma, Y.; Gao, X.; et al. Stretchable ultrasonic arrays for the three-dimensional mapping of the modulus of deep tissue. *Nat. Biomed. Eng.* **2023**, *7*, 1321-34. DOI PubMed
6. Wang, C.; Li, X.; Hu, H.; et al. Monitoring of the central blood pressure waveform via a conformal ultrasonic device. *Nat. Biomed. Eng.* **2018**, *2*, 687-95. DOI PubMed PMC
7. Han, H.; Ma, X.; Deng, W.; et al. Imaging-guided bioresorbable acoustic hydrogel microrobots. *Sci. Robot.* **2024**, *9*, eadp3593. DOI PubMed
8. Tong, X.; Liu, C. Z.; Luo, Y.; et al. Panoramic photoacoustic computed tomography with learning-based classification enhances breast lesion characterization. *Nat. Biomed. Eng.* **2025**, *10*, 161-77. DOI PubMed PMC

9. Zhang, Q.; Liang, X.; Zhang, Y.; Nie, H.; Chen, Z. A review of contrast-enhanced ultrasound using SonoVue® and Sonazoid™ in non-hepatic organs. *Eur. J. Radiol.* **2023**, *167*, 111060. DOI PubMed
10. Marsico, M.; Gabbani, T.; Casseri, T.; Biagini, M. R. Factors predictive of improved abdominal ultrasound visualization after oral administration of simethicone. *Ultrasound. Med. Biol.* **2016**, *42*, 2532-7. DOI PubMed
11. Liu, J.; Liu, N.; Xu, Y.; et al. Bioresorbable shape-adaptive structures for ultrasonic monitoring of deep-tissue homeostasis. *Science* **2024**, *383*, 1096-103. DOI PubMed
12. Li, Z.; Yang, D.; Liu, S.; et al. Broadband gradient impedance matching using an acoustic metamaterial for ultrasonic transducers. *Sci. Rep.* **2017**, *7*, 42863. DOI PubMed PMC
13. Ma, G.; Sheng, P. Acoustic metamaterials: from local resonances to broad horizons. *Sci. Adv.* **2016**, *2*, e1501595. DOI PubMed PMC
14. Cummer, S. A.; Christensen, J.; Alù, A. Controlling sound with acoustic metamaterials. *Nat. Rev. Mater.* **2016**, *1*, 16001. DOI
15. Lemoult, F.; Fink, M.; Lerosey, G. Acoustic resonators for far-field control of sound on a subwavelength scale. *Phys. Rev. Lett.* **2011**, *107*, 064301. DOI PubMed
16. Lemoult, F.; Kaina, N.; Fink, M.; Lerosey, G. Wave propagation control at the deep subwavelength scale in metamaterials. *Nat. Phys.* **2012**, *9*, 55-60. DOI
17. Boccaccio, M.; Rachiglia, P.; Malfense Fierro, G. P.; Pio Pucillo, G.; Meo, M. Deep-subwavelength-optimized holey-structured metamaterial lens for nonlinear air-coupled ultrasonic imaging. *Sensors* **2021**, *21*, 1170. DOI PubMed PMC
18. Zhang, M.; Jin, B.; Hua, Y.; et al. Reconfigurable dynamic acoustic holography with acoustically transparent and programmable metamaterial. *Nat. Commun.* **2025**, *16*, 9126. DOI PubMed PMC
19. Jia, Y.; Zhang, S.; Zhang, X.; et al. Compact meta-differentiator for achieving isotropically high-contrast ultrasonic imaging. *Nat. Commun.* **2024**, *15*, 2934. DOI PubMed PMC
20. Zhou, Y.; Zheng, H.; Kravchenko, I. I.; Valentine, J. Flat optics for image differentiation. *Nat. Photonics.* **2020**, *14*, 316-23. DOI
21. Mei, J.; Ma, G.; Yang, M.; Yang, Z.; Wen, W.; Sheng, P. Dark acoustic metamaterials as super absorbers for low-frequency sound. *Nat. Commun.* **2012**, *3*, 756. DOI PubMed
22. Ma, G.; Yang, M.; Xiao, S.; Yang, Z.; Sheng, P. Acoustic metasurface with hybrid resonances. *Nat. Mater.* **2014**, *13*, 873-8. DOI PubMed
23. Yang, M.; Chen, S.; Fu, C.; Sheng, P. Optimal sound-absorbing structures. *Mater. Horiz.* **2017**, *4*, 673-80. DOI
24. Zhang, K.; Ma, C.; He, Q.; et al. Metagel with broadband tunable acoustic properties over air-water-solid ranges. *Adv. Funct. Mater.* **2019**, *29*, 1903699. DOI
25. Dong, E.; Song, Z.; Zhang, Y.; et al. Bioinspired metagel with broadband tunable impedance matching. *Sci. Adv.* **2020**, *6*, eabb3641. DOI PubMed PMC
26. Tian, Y.; Yang, Y.; Wang, J.; et al. Biodegradable ultrasound contrast tape for tracing intestinal motility. *Nat. Commun.* **2025**, *16*, 7910. DOI PubMed PMC
27. Zhang, J.; Zhou, N.; Dong, E.; et al. Soft bio-metamaterials with high acoustic transparency and gradient refractive index for tunable acoustic beamformer. *Matter* **2024**, *7*, 3857-75. DOI
28. Jin, Y.; Kumar, R.; Poncelet, O.; Mondain-monval, O.; Brunet, T. Flat acoustics with soft gradient-index metasurfaces. *Nat. Commun.* **2019**, *10*, 143. DOI PubMed PMC
29. Chen, Q.; Zhang, B.; Bai, Y.; Wang, L.; Rejab, M. R. M. Review of Phononic crystals and acoustic metamaterials. *IOP. Conf. Ser. Mater. Sci. Eng.* **2020**, *788*, 012052. DOI
30. Yuk, H.; Varela, C. E.; Nabzdyk, C. S.; et al. Dry double-sided tape for adhesion of wet tissues and devices. *Nature* **2019**, *575*, 169-74. DOI PubMed